ADVANCED FUNCTIONAL MATERIALS
www.afm-journal.de

Self-Powered Triboelectric Sensor for Real-Time, Intelligent Occlusal Force Monitoring

Yan Du, Jingkai Song, Houfang Liu, Zhiwei Zhang, Bing Han, Xuliang Deng, Tianling Ren,* Zhong Lin Wang,* and Di Wei**

Occlusal force is a critical biomechanical parameter in orthodontics, implant restoration, and temporomandibular joint evaluation. However, its multidimensional dynamics and the complex intraoral environment pose significant challenges to existing sensing technologies, which often lack the capacity for real-time, high-resolution, and non-invasive monitoring. Here, a self-powered triboelectric sensor (STS) is introduced for autonomous, 3D occlusal force monitoring. The device features a multilayer soft-contact architecture comprising a Poly(vinylidene fluoride-co-hexafluoropropylene (PVDF-HFP)/Barium titanate ($BaTiO_3$) composite dielectric layer, flexible polyurethane (PU) foam, and carbon–silicone composite electrodes, enabling conformal integration and precise biomechanical signal acquisition. This configuration enables fully self-powered, real-time acquisition of occlusal force magnitude, frequency, and spatial distribution. The conformal soft interface facilitates adaptive sensing of multidimensional force vectors across complex intraoral geometries, allowing high-fidelity reconstruction of dynamic occlusal mechanics. An optimized multichannel architecture improves spatial resolution and surface conformity, enabling accurate tracking of contact trajectories and force distributions during occlusion. Coupled with artificial intelligence, the system performs real-time signal analysis and abnormal pattern recognition, achieving classification accuracies of 98.75% for occlusal frequency and 98.71% for bite force magnitude. By integrating triboelectric sensing into a compliant occlusal interface, this platform redefines digital occlusal monitoring and offers a scalable path toward intelligent, data-driven occlusal healthcare.

1. Introduction

Occlusal force is a key biomechanical parameter that reflects the functional integrity of the craniofacial system and plays a central role in clinical practices such as orthodontic treatment, implant restoration, and temporomandibular disorder assessment.[1] With the rise of digital dentistry and precision medicine, clinical demands have evolved toward real-time acquisition, high-dimensional analysis, and intuitive visualization of occlusal data. In complex, individualized treatment scenarios, capturing dynamic features of occlusal force, including magnitude, frequency, and spatial distribution, is essential for timely intervention and therapeutic optimization.[2] However, the occlusion process involves temporally sequenced, multidirectional force interactions and significant spatial variability. These challenges are compounded by intraoral constraints such as limited space, high humidity, and localized stress concentrations. Existing technologies fall short of meeting the combined requirements for high resolution, dynamic responsiveness, and seamless, noninvasive integration, highlighting a substantial gap

Y. Du, Z. Zhang, Z. L. Wang, D. Wei
Beijing Institute of Nanoenergy and Nanosystems
Chinese Academy of Sciences
Beijing 101400, China
E-mail: zlwang@binn.cas.cn; weidi@binn.cas.cn

Y. Du
School of Nanoscience and Engineering
University of Chinese Academy of Sciences
Beijing 100049, China

J. Song, H. Liu, T. Ren
School of Integrated Circuits & Beijing National Research Center for Information Science and Technology
Tsinghua University
Beijing 10084, China
E-mail: RenTL@tsinghua.edu.cn

The ORCID identification number(s) for the author(s) of this article can be found under https://doi.org/10.1002/adfm.202519646

DOI: 10.1002/adfm.202519646

B. Han
Department of Cariology and Endodontology
National Center for Stomatology
National Clinical Research Center for Oral Diseases
National Engineering Research Center of Oral Biomaterials and Digital Medical Devices
Beijing Key Laboratory of Digital Stomatology
Peking University School and Hospital of Stomatology
Beijing 100081, China

X. Deng
Department of Geriatric Dentistry
Peking University School and Hospital of Stomatology
Beijing 100081, China
E-mail: kqdengxuliang@bjmu.edu.cn

D. Wei
Centre for Photonic Devices and Sensors
University of Cambridge
9 JJ Thomson Avenue, Cambridge CB3 0FA, UK

between accurate occlusal force measurement and real-time clinical application.

The T-SCAN system remains the most clinically adopted digital occlusal analysis platform, employing a high-density resistive sensor array (62 sensors cm^{-2}) to capture occlusal contact sequence, timing, and relative force distribution.[3] However, its rigid, planar polyester sensing film fails to conform to the 3D topology of occlusal surfaces, leading to underestimation of actual contact areas and trajectories. Critically, the system lacks the capability to resolve true force magnitudes and multidirectional vectors, and cannot perform continuous, high-fidelity tracking of dynamic occlusal interactions. These limitations substantially constrain its applicability in complex, real-time diagnostic environments. In contrast, intraoral 3D scanning systems reconstruct static anatomical geometries with high precision using optical stitching algorithms, facilitating structural assessments.[4] Nonetheless, they are inherently limited to morphology acquisition and cannot capture dynamic mechanical responses such as force magnitude, directionality, or temporal evolution under load. Their high system complexity and cost further impede routine deployment in decentralized clinical settings. Given the technical limitations of commercial systems in capturing dynamic, multidimensional force distributions with real-time continuity, recent efforts have focused on the development of flexible sensors leveraging piezoelectric[5] and piezoresistive[6] mechanisms for occlusal force monitoring. Typically constructed from polymeric piezoelectric films or conductive composites, these devices offer moderate sensitivity and are potentially suitable for intraoral use.[7] However, most remain restricted to uniaxial or planar sensing modalities, rendering them insufficient for resolving the complex, vectorial force fields characteristic of occlusal dynamics. Their reliance on external power supplies and bulky signal conditioning units compromises system integration, reduces energy efficiency, and limits long-term autonomous operation within the constrained intraoral space.[8] To enhance signal output, multilayer stacking and rigid structural designs are often employed, sacrificing mechanical compliance and occlusal conformability, which adversely affects wearability and signal fidelity.[9] Furthermore, repeated high-frequency loading during mastication leads to signal drift, mechanical fatigue, and long-term performance degradation, impeding continuous dynamic monitoring.[10] To address these challenges, triboelectric nanogenerator (TENG)[11] technology has emerged as a transformative solution, offering self-powered operation,[12] high mechanical flexibility,[13] multidimensional force sensing,[14] and intrinsic adaptability[15] to the complex mechanical environment of the oral cavity. TENG-based systems provide a promising pathway toward intelligent, real-time, 3D occlusal monitoring, enabling the next generation of smart, data-driven dental platforms.[16]

Herein, we propose a noninvasive, self-powered triboelectric sensor (STS) for 3D monitoring of occlusal forces. The device integrates a multilayer soft-contact interface composed of a PVDF-HFP/$BaTiO_3$ composite dielectric layer, flexible PU, and carbon-silicone electrodes, enabling continuous acquisition of occlusal force magnitude and frequency without external power supply. The conformal soft interface permits adaptive sensing of multidimensional force vectors across complex intraoral geometries, supporting high-fidelity reconstruction of dynamic occlusal mechanics. Multi-channel layout and optimized electrode spacing further enhance spatial resolution, enabling precise mapping of occlusal contact trajectories and force evolution. Designed for complex intraoral conditions, the system exhibits excellent biocompatibility and robust operational stability. When integrated with machine learning algorithms, it enables real-time interpretation of occlusal data streams and facilitates individualized diagnostics and adaptive therapeutic interventions. This triboelectric sensing strategy overcomes key limitations of conventional 2D force sensing, advancing the development of intelligent, miniaturized, and clinically scalable dental technologies.

2. Results and Discussion

2.1. Design of the STS-Based Occlusal Biomechanics Monitoring System

The system framework of the STS for in situ occlusal force monitoring is schematically presented in **Figure 1a**, and its 3D structural layout is depicted in Figure 1b. The raw data acquired by the STS could be further processed using machine learning algorithms to extract clinically relevant patterns, providing intelligent feedback to dental practitioners for real-time diagnosis and personalized treatment planning. The STS was developed to address the biomechanical complexity and spatial constraints of the occlusal environment, where continuous deformation, multidirectional force coupling, and high-frequency occlusal stimuli are commonly encountered. To ensure reliable signal transduction under these dynamic conditions, a multilayer soft contact structure was constructed, integrating mechanical adaptability, triboelectric energy conversion, and stable charge collection capability. The STS was composed of three primary functional layers. At the top, a PU layer was employed as a compressible buffer substrate.[17] The PU not only accommodated occlusal deformation by providing elasticity and shape recovery, but also ensured conformal contact between the opposing surfaces during bite events, which was essential for consistent triboelectric interaction (Figure S1, Supporting Information). Beneath this layer, a dielectric layer made of a PVDF-HFP/$BaTiO_3$ served as the composite dielectric layer.[18] This composite was selected due to its excellent dielectric permittivity and its ability to form abundant interfacial polarization centers. The inclusion of $BaTiO_3$ promoted the transformation of PVDF-HFP into the electroactive β phase, thereby enhancing both the triboelectric charge generation and the mechanical to electrical conversion efficiency.[19] At the bottom, a layer of carbon-silicone electrodes was used to collect the generated charges. Energy spectrum analysis revealed the elemental composition of the carbon-silicone electrode, as shown in Figure S2 (Supporting Information). This material combined flexibility, conductivity, and occlusal biocompatibility, making it suitable for integration in wearable intraoral devices.[20] To facilitate multidimensional force detection, the structural configuration was optimized to support distributed loading and spatial deformation. The compressibility of the PU layer enabled vertical displacement sensing, while lateral forces introduced tangential movement and shear induced triboelectric generation. Together, these effects allowed the STS to transduce complex occlusal behaviors into high-resolution electrical signals.

Representative clinical application scenarios of the STS system are illustrated in Figure 1c. In autonomous oral health

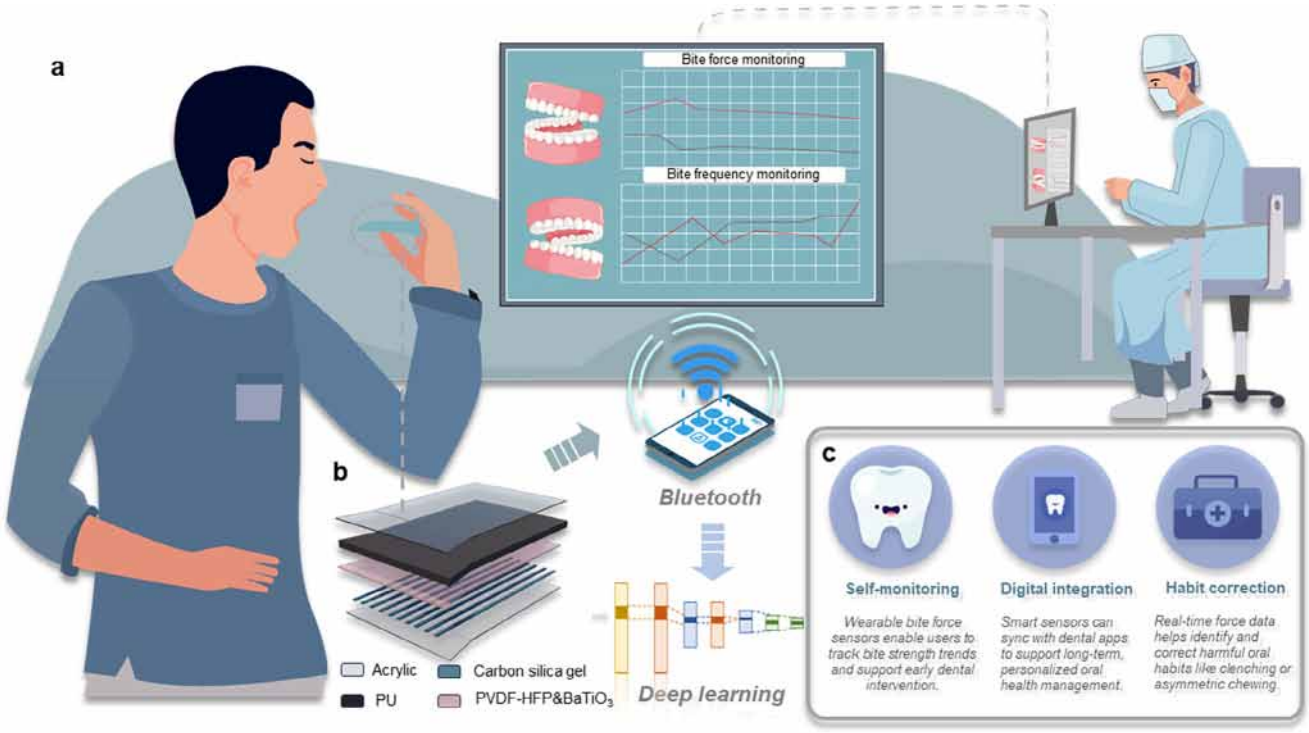

Figure 1. Schematic illustration of the STS-based occlusal monitoring system. a) Conceptual diagram of real-time occlusal force sensing. b) Structural diagram of the STS. c) Representative clinical application scenarios of the STS system for dynamic and multidimensional occlusal force monitoring.

tracking, the STS was envisioned to allow users to continuously track bite force variations during daily occlusal activities, enabling early identification of functional disorders such as bruxism or occlusal imbalance. When integrated with digital platforms, the device could support longitudinal data acquisition and cloud-based analytics, promoting personalized dental health management. Furthermore, the ability to dynamically capture real-time occlusal force profiles offered opportunities for behavioral correction, such as identifying unilateral chewing habits or excessive clenching forces and prompting timely intervention. In summary, the STS system was structurally engineered to meet the key requirements of occlusal biomechanical sensing: high flexibility, spatial adaptability, material biocompatibility, and self powered electrical output. The integration of advanced dielectric materials and multilayer design principles laid a solid foundation for dynamic, multidirectional, and clinically relevant occlusal force monitoring.

2.2. Operational Principles and Simulation of the STS

The electron transfer mechanism during the operation of the STS is illustrated in **Figure** 2a. In the absence of occlusal pressure, the PVDF-HFP/$BaTiO_3$ composite dielectric layer was in an initial contact state with the carbon-silicone composite electrodes. Due to differences in electronegativity of surface materials, the PVDF-HFP/$BaTiO_3$ composite dielectric layer tended to gain electrons and became negatively charged, while the carbon-silicone electrodes tended to lose electrons and acquired a positive charge, resulting in an initial charge distribution at the interface. When vertical occlusal pressure was applied, the PU buffer layer underwent mechanical deformation due to its intrinsic flexibility, thereby establishing increased contact with the dielectric layer. This interaction induced further triboelectric charge generation. Simultaneously, a potential difference developed between the PVDF-HFP/$BaTiO_3$ composite dielectric layer and the carbon-silicone electrodes, leading to the flow of electrons from the ground to the electrode, which generated a transient current. The intensity of this current correlated positively with the applied occlusal force. As the pressure reached its peak, charge transfer was completed, and the current gradually decreased to zero. At the microscale, the contact between the material surfaces was not perfectly uniform due to the existence of interfacial air gaps. As occlusal force continued to increase, the soft interface between the PU layer and the carbon-silicone electrodes underwent further compression. This resulted in more effective contact between the dielectric and electrode layers, leading to secondary charge excitation and current compensation. Such effects contributed to enhanced signal stability and improved pressure sensitivity, as schematically illustrated in Figure 2b.

To further investigate the dynamic behavior of the STS under mechanical loading, finite element simulations were conducted using COMSOL Multiphysics. The displacement field evolution of the STS under compressive force was simulated and is presented in Figure 2c, through which the mechanical deformation profile of the layered structure over time was demonstrated. In addition, the spatial distribution of electric potential within the STS structure as a function of applied pressure is presented in Figure 2d, demonstrating that the potential increases with pressure and gradually stabilizes as the dielectric–electrode interface

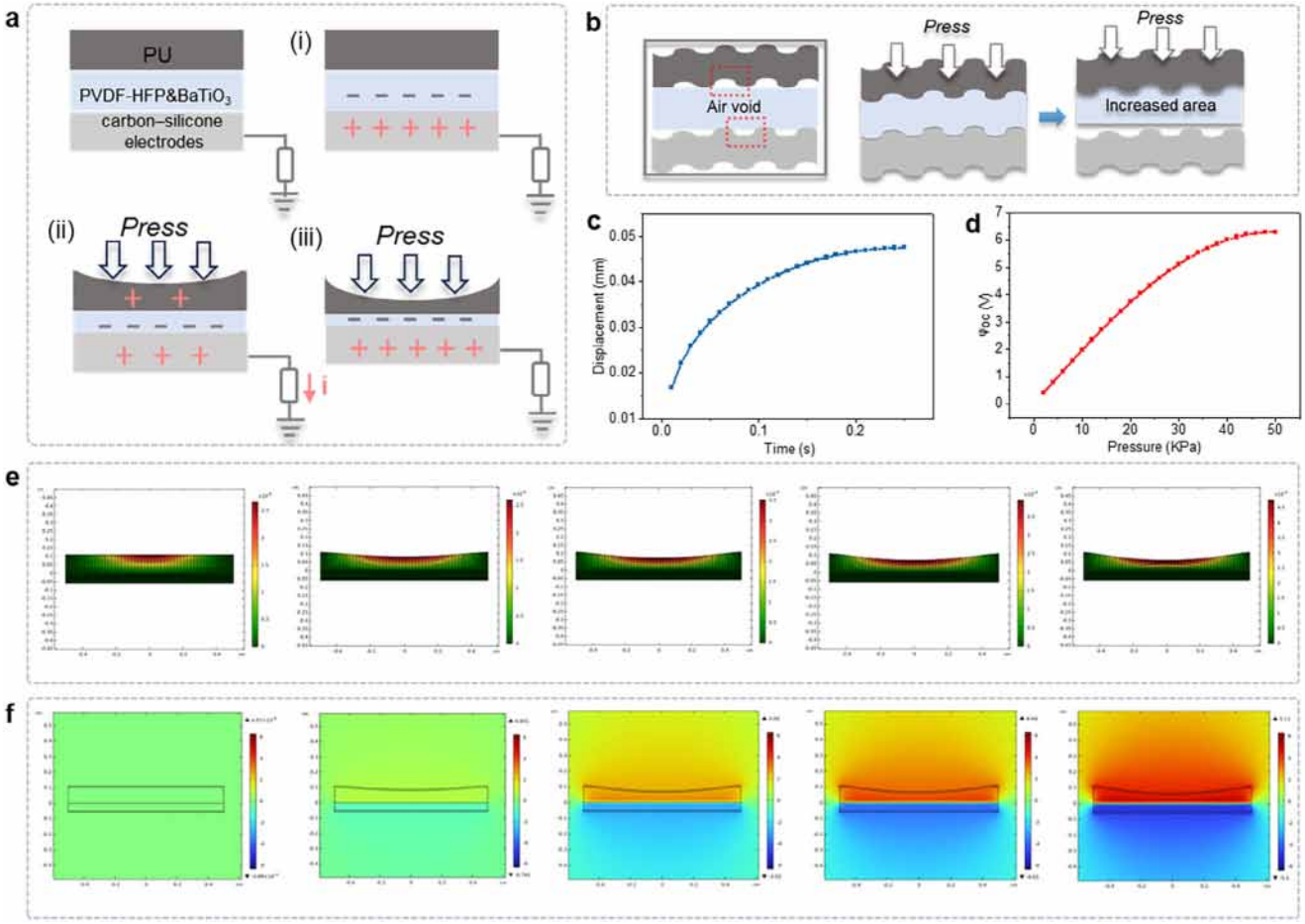

Figure 2. Working mechanism and simulation analysis of the STS. a) Schematic diagram of the electron transfer process during STS operation. b) Illustration of the soft contact interface of the STS. c) COMSOL-simulated displacement profile of the STS over time. d) COMSOL-simulated electric potential variation of the STS under different pressures. e) Illustration of STS displacement variation simulated by COMSOL. f) Illustration of STS electric potential variation under pressure simulated by COMSOL.

approaches full contact. Further simulated results are displayed in Figure 2e, where the displacement variation of the STS structure under pressure was visualized, providing a detailed perspective on the deformation pathways. The electric potential distribution of the STS structure under compressive loading is illustrated in Figure 2f. The potential gradient increased progressively with applied pressure, reflecting the evolution of charge separation at the interface. In this simulation, the model was based on triboelectrification, considering the variation of interfacial contact area and the resulting potential distribution, thereby capturing the formation of interfacial charges and the development of potential differences. These simulation results collectively validated the proposed working mechanism and provided strong theoretical support for the experimental observations.

In summary, the working mechanism of the STS involves a synergistic interaction between material deformation, triboelectric charge generation, and dynamic electron transfer processes, all of which are strongly influenced by the applied mechanical pressure. The introduction of a soft PU buffer layer not only enhances conformal contact but also contributes to secondary charge excitation, thereby improving the device's sensitivity and signal stability. The COMSOL-based finite element simulations offer valuable insights into the mechanical and electrical responses of the device, effectively supporting the proposed theoretical model. Together, the experimental and simulation results provide a comprehensive understanding of the pressure sensing behavior of the STS, laying a solid foundation for its application in intelligent occlusal health monitoring systems.

2.3. Optimizing Signal Output of the Self-Powered Triboelectric Sensing System

To characterize the electrical behavior of the STS and identify key parameters influencing its performance, a single-channel prototype was fabricated and systematically evaluated under controlled compressive conditions. As shown in **Figure 3**a, the device adopted a multilayer architecture consisting of an acrylic substrate, a PVDF-HFP/$BaTiO_3$ composite dielectric layer, a compressible PU buffer, and a pair of flexible carbon–silicone electrodes. This configuration was designed to accommodate vertical force transmission while maintaining mechanical

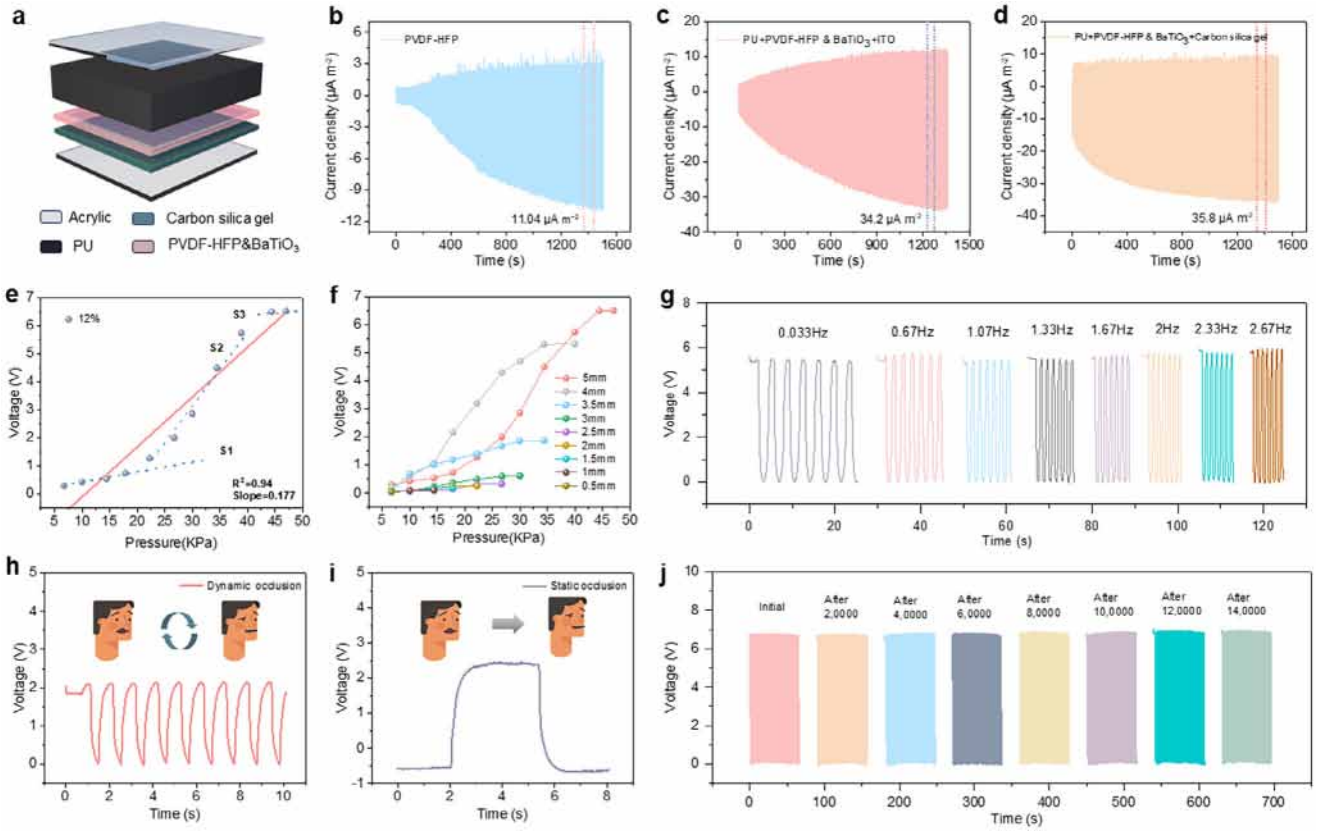

Figure 3. Parameter optimization and output performance of the STS. a) Schematic illustration of the 3D structure of the single-channel STS. b) Current density of the STS using a PVDF-HFP dielectric layer and ITO as the output electrode. c) Current density of the STS using a PVDF-HFP/$BaTiO_3$ composite dielectric layer and ITO electrode. d) Current density of the STS using a PVDF-HFP/$BaTiO_3$ composite dielectric layer and carbon–silicone composite electrode. e) Output voltage of the STS with 12 wt.% $BaTiO_3$ doping under different applied pressures. f) Output voltage of the STS with different PU layer thicknesses under varying pressures. g) Output voltage response of the STS under various excitation frequencies. h) Dynamic occlusion output voltage response of the STS. i) Static occlusion output voltage response of the STS. j) Stability test of the STS under repeated mechanical loading.

compliance for occlusal applications. To simulate occlusal loading, a programmable linear motor was employed to apply periodic compressive forces with controlled amplitude and frequency, enabling precise replication of dynamic bite scenarios.

As a baseline, we first fabricated a reference STS comprising a pure PVDF-HFP dielectric layer and indium tin oxide (ITO) electrodes. The output voltage response under stepwise pressure loading is presented in Figure S3 (Supporting Information), which showed a monotonic increase in voltage with increasing pressure, along with a linear profile in the low-to-moderate pressure range. The corresponding current density output is shown in Figure 3b, where a saturation value of 11.04 $\mu A \cdot m^{-2}$ was reached at ≈1400 s, indicating a stable charge transfer process and repeatable triboelectric interaction at the contact interface. However, the limited dielectric polarization of the pristine PVDF-HFP layer restricted further enhancement of the output signal. To address this limitation, we introduced $BaTiO_3$ nanoparticles into the PVDF-HFP matrix to form a composite dielectric. The incorporation of $BaTiO_3$ was aimed at improving the dielectric constant and promoting β-phase formation in PVDF-HFP, thereby enhancing dipole alignment and interfacial polarization. Its inherent ferroelectric properties have been reported to enhance interfacial polarization and electrostatic charge storage, thereby strengthening charge trapping within the dielectric layer.[21]

This structural modification led to noticeable improvements in the output response, as evidenced by the current density curve shown in Figure 3c, which exhibited a faster rise and earlier saturation compared to the undoped counterpart. In addition, the voltage–pressure relationship demonstrated enhanced linearity and magnitude across a broader pressure range (Figure S4, Supporting Information). This enhancement can be attributed to the intrinsic piezoelectricity of PVDF-HFP and the further increase in dielectric polarization and effective piezoelectric coefficient provided by the incorporation of $BaTiO_3$ nanoparticles. Under mechanical loading, the induced piezoelectric polarization of the composite layer further increased the overall output performance (Figure S5, Supporting Information). Consequently, the voltage enhancement could be attributed to a dual mechanism: first, an enhanced triboelectric effect, resulting from improved dielectric constant and interfacial contact that promoted more efficient charge separation; second, synergistic piezoelectric polarization, which reinforced the effective polarization and charge retention of the composite.[22] To further optimize the electrode interface, the rigid ITO was replaced with a flexible carbon–silicone composite. This substitution was intended to enhance mechanical

conformity, reduce interfacial mismatch, and improve biocompatibility. As shown in Figure 3d, the use of a soft electrode led to a faster current response, with saturation achieved in a shorter time frame. The overall output amplitude was also slightly increased, likely due to improved contact intimacy and more efficient triboelectric charge transfer enabled by the dual soft–soft interface between the PU layer and the flexible electrode.

The effect of $BaTiO_3$ doping concentration on electrical output was then systematically investigated by fabricating composite dielectric layers containing 3, 6, 9, 12, and 15 wt.% $BaTiO_3$. As depicted in Figure 3e and Figure S6 (Supporting Information), the output voltage exhibited a doping-dependent behavior, reaching a maximum at 12 wt.%. Below this concentration, insufficient dipole polarization limited signal generation, while higher concentrations (e.g., 15 wt.%) likely led to particle agglomeration, increased internal dielectric loss, and reduced uniformity of the composite layer. The 12 wt.% composition also yielded the best fit to a second-order sensitivity between voltage and pressure, which is favorable for sensing nonlinear mechanical inputs typically associated with occlusal contact. The mechanical configuration of the PU buffer layer was also evaluated as a functional design parameter. By varying the thickness of the PU layer, we observed distinct differences in device output. As shown in Figure 3f and Figure S7 (Supporting Information), thicker PU layers improved pressure absorption but simultaneously dampened the effective triboelectric interaction due to reduced compressive deformation under moderate forces. Among the tested configurations, a 5 mm PU layer provided a suitable trade-off between mechanical cushioning and electrical sensitivity, while also maintaining structural compactness suitable for intraoral integration.

The frequency response of the optimized STS was examined under different excitation frequencies to assess dynamic signal stability. As shown in Figure 3g, the output voltage remained consistent across a broad range of frequencies, indicating the device's ability to respond reliably to variable-rate mechanical inputs. This characteristic was particularly important for capturing occlusal patterns during chewing, which occurred at different temporal scales. To evaluate the STS under more application-relevant conditions, measurements simulating both dynamic and static occlusion were performed. The corresponding voltage signals are presented in Figure 3h,i, respectively. The device exhibited distinct and stable output profiles in both modes, validating its capability to differentiate between static force maintenance and transient force variation, which was critical for comprehensive occlusal analysis. Moreover, charge decay tests were conducted on the STS under a constant static load to evaluate the influence of dielectric materials on static signal retention. The results show that the device with a pure PVDF-HFP dielectric decayed to 0.40 V within ≈350 s, whereas the PVDF-HFP/$BaTiO_3$ composite dielectric device maintained 0.46 V at 600 s. Control experiments further confirm that $BaTiO_3$ nanoparticles, by forming polarization centers within the dielectric layer, significantly enhance charge trapping and retention, thereby delaying charge decay. In essence, the voltage signal of the STS under static loading fundamentally arises from charge decay, not continuous charge generation. Nevertheless, the polarization-enhanced dielectric layer combined with the stable soft–soft interface structure significantly prolongs charge retention and signal duration. This improvement allows the STS to maintain measurable static voltage longer than conventional triboelectric/piezoelectric sensors, providing a practical advantage for applications such as oral occlusion monitoring, where static force detection is required (Figure S8, Supporting Information). To further evaluate the STS's response to forces applied in multiple directions, in addition to the primary loading direction (normal force), lateral (shear) forces were applied to the STS, and the corresponding output voltages were recorded and analyzed (Figure S9, Supporting Information). The results clearly demonstrate that the STS generates stable signals under both normal and shear loading conditions, thereby confirming its reliable detection of full-vector force components.

Finally, the long-term mechanical durability of the STS was assessed through repetitive cyclic loading. As shown in Figure 3j, the electrical output remained stable over 140 000 compression-release cycles, with no significant signal degradation. This stability is attributed to the combined effects of: 1) the uniform 12 wt.% $BaTiO_3$ dielectric layer minimizing particle agglomeration and maintaining consistent dipole polarization; 2) the flexible PU buffer layer absorbing stress and ensuring stable interfacial contact between the dielectric and electrode layers, thereby preserving consistent triboelectric charge transfer during repeated loading. To evaluate its practical applicability, the performance of the STS was tested under various simulated oral conditions. Within a temperature range of 5–55 °C, the STS output voltage decreased slightly from 6.8 to 6.4 V (Figure S10a, Supporting Information), and under high humidity (95–100 % RH), it decreased from 5.5 to 5.1 V (Figure S10b, Supporting Information). These results indicate that although extreme temperature and humidity cause minor variations in the output, the overall performance of the STS remains stable. Furthermore, cycling tests conducted at 37 °C and 97 % RH for 150 000 cycles demonstrated 84.3 % retention of the initial signal (Figure S11, Supporting Information), confirming the STS's long-term reliability and its potential for practical oral applications. This stability can be attributed to the STS's conformal contact design, which ensures consistent mechanical engagement, in combination with the composite material's high dielectric constant enhancing the triboelectric effect and its strong piezoelectric polarization, collectively enabling robust and reliable electrical output.

These findings collectively underscore the critical role of material composition, interfacial design, and structural configuration in modulating the electrical performance of the STS. By integrating a composite dielectric layer, soft–soft contact interfaces, and optimized mechanical buffering, the device achieved enhanced signal amplitude, faster response kinetics, and stable long-term operation. This performance foundation enables the STS to serve not only as a passive mechanical transducer but also as a reliable front-end platform for intelligent occlusal monitoring systems.

2.4. Intelligent Occlusal Force Mapping Enabled by Multi-Channel Triboelectric Sensor System

To demonstrate the feasibility of spatially resolved occlusal force monitoring, a multi-channel STS system was developed and tested. This prototype incorporated ten independent sensing channels, each capable of real-time pressure detection, enabling

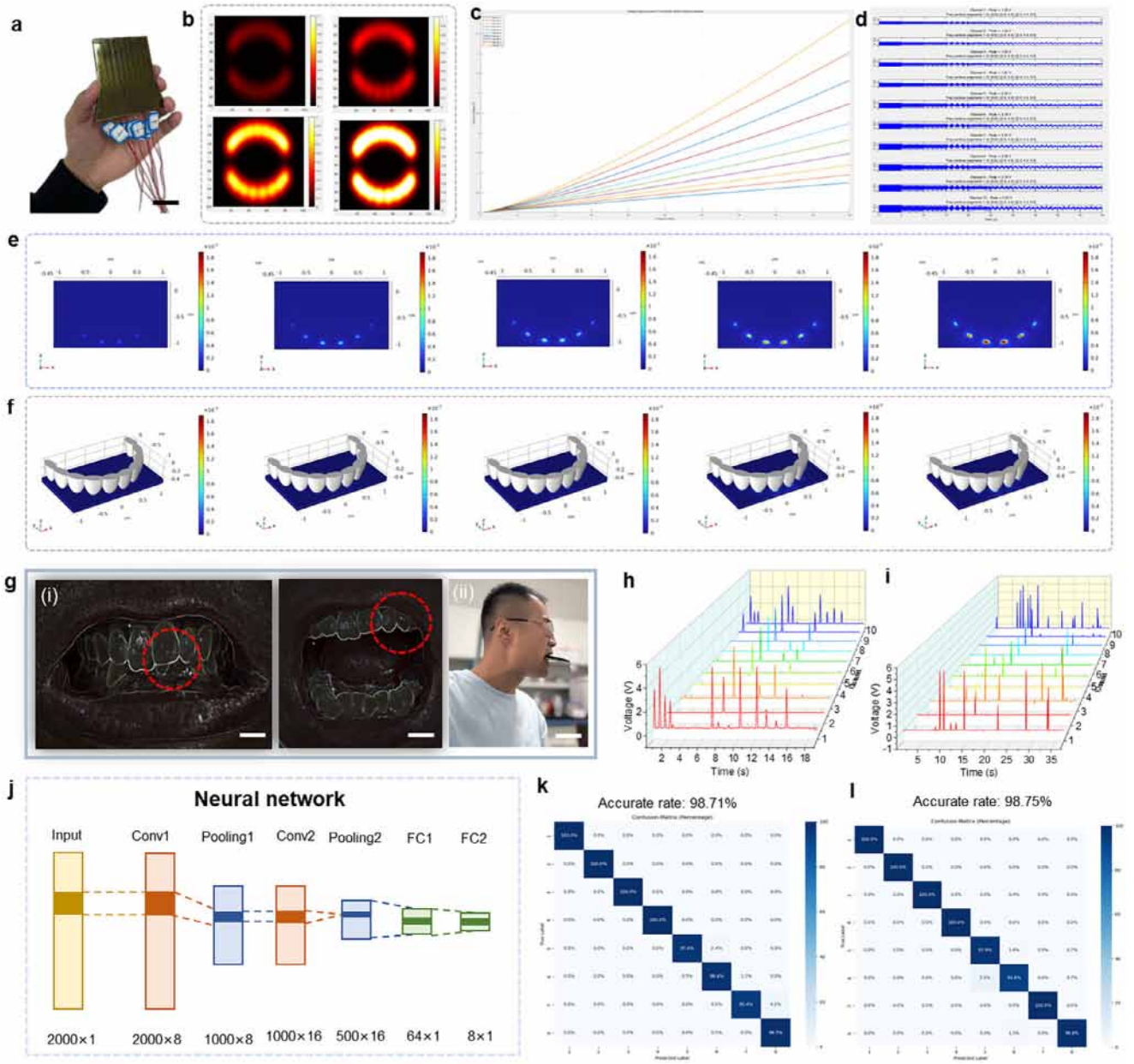

Figure 4. Practical application of the multi-channel STS. a) Image of the multi-channel STS. b) Occlusion heat map generated by MATLAB. c) Output voltage under varying occlusion forces. d) Output voltage under varying occlusion frequencies. e) 2D top view of the occlusal pressure distribution simulated by COMSOL for the STS. f) 3D frontal view of the occlusal pressure distribution simulated by COMSOL for the STS. g) Subject with misaligned teeth: i) intraoral photograph of the dentition; ii) photograph of the subject biting on the multi-channel STS. h) Output voltage of the multi-channel STS under different occlusal forces applied by the subject. i) Output voltage of the multi-channel STS under different occlusal frequencies applied by the subject. j) Architecture of the convolutional neural networks (CNNs) used for data classification. k) Confusion matrix for occlusal force classification results. l) Confusion matrix for occlusal frequency classification results.

simultaneous multipoint acquisition and generation of a full occlusal force distribution map. The physical layout of the multi-channel sensor array is shown in **Figure** 4a.

We further investigated the output performance of the multi-channel STS at varying electrode spacings. Five configurations were evaluated, with electrode gaps set at 0.5, 1.0, 1.5, 2.0, and 2.5 mm. As illustrated in Figure S12 (Supporting Information), the output voltage increased progressively from 0.5 to 2.0 mm, which was attributed to the expansion of the effective strain zone within the dielectric layer, thereby enhancing charge separation efficiency. However, at 2.5 mm, a noticeable drop in signal amplitude was observed. This decline may have resulted from reduced contact area and weakened local electric field intensity, both of which compromised the efficiency of triboelectric charge induction. Taking into account both output performance and array density, a spacing of 2.0 mm was selected as

the optimal configuration, balancing sensitivity and device integration. The integration of multiple sensing units with optimized electrode spacing significantly improved the spatial resolution of occlusal force acquisition. This spatially distributed architecture provided a robust data foundation for future incorporation with machine learning algorithms for multidimensional occlusal pattern recognition and personalized diagnostic modeling.

To validate the system's utility in mimicking real occlusal conditions, a testing platform was constructed that included a dental model, a programmable linear motor, and the multi-channel STS sensor array. The testing platform simulating occlusal occlusion is illustrated in Figure S13 (Supporting Information), and the tooth model is shown in Figure S14 (Supporting Information). The multi-channel STS enabled real-time, spatially resolved acquisition of occlusal force data, allowing dynamic visualization and mapping of bite pressure distribution with high temporal fidelity. Such intelligent, real-time monitoring facilitates the capture of complex occlusal interactions as they naturally occur during mastication. Occlusal heat maps generated from the multichannel outputs via MATLAB analysis are presented in Figure 4b, revealing localized force concentrations across simulated biting surfaces. The simulated occlusion output from all 10 channels is further summarized in Figure 4c, demonstrating the system's ability to resolve spatial differences in bite force magnitude.

Additionally, the STS signals were correlated with geometric occlusal data obtained through digital tooth scanning. These data were integrated into COMSOL Multiphysics to simulate 3D occlusal stress distributions, providing an advanced, spatially precise, and quantitative assessment of bite forces across the dentition. This intelligent 3D modeling enhances understanding of biomechanical load transfer and supports personalized occlusal diagnostics. The simulated stress field is presented in Figure 4e,f, providing a visual representation of bite pressure distribution across the dentition.

To assess interoral performance, a pilot study was conducted with a volunteer presenting with mild dental malalignment. The STS sensor array was directly affixed to the dentition, and the participant was instructed to perform a series of voluntary biting actions (Figure 4g). During use, the sensor remained stably attached, with no reported discomfort or interference with natural occlusion, confirming its noninvasive and wearable characteristics. Real-time voltage signals were successfully acquired during bite closure, as shown in Figure 4h, with a clear correlation between voltage amplitude and occlusal force magnitude. Furthermore, chewing frequency monitoring was performed by instructing the subject to execute repetitive masticatory cycles over a fixed time window. The STS produced a continuous, periodic signal pattern corresponding to each bite cycle (Figure 4i), allowing precise identification of chewing rhythm and frequency. These results confirmed the STS's capacity to dynamically monitor both the magnitude and temporal characteristics of occlusal activity in real occlusal environments. To comprehensively assess the multichannel STS's performance in realistic oral environments, tests were conducted under various occlusion scenarios, including anterior bite, posterior bite, and alternating bite. These experiments enabled a systematic evaluation of the multi-channel STS's response to forces applied at different positions, directions, and distributions, thereby verifying its multi-directional force sensing capability and robustness under complex oral conditions (Figure S15, Supporting Information).

To explore the potential of the STS system for intelligent occlusal behavior classification, a series of machine learning experiments was conducted using data collected from the multichannel sensor array. The raw signals were acquired at a sampling frequency of 1000 Hz, with each recording lasting ≈30 s. Two functional tasks were designed for classification: bite force magnitude discrimination and frequency pattern recognition. Each task comprised eight distinct classes, and three independent recordings were collected for each class. Given the extended duration of the recordings and the presence of low-frequency baseline drift in the sensor signals, preprocessing was applied prior to neural network training. Each raw signal was segmented into shorter windows and baseline-corrected to improve classification robustness. For the bite force classification task, recordings were segmented into 3-s intervals (3000 data points per segment), while 2-s intervals were used for frequency classification. To mitigate baseline drift, the mean value of each segment was subtracted from the corresponding data points. Following this preprocessing pipeline, data augmentation was performed using a sliding-window approach, resulting in 1935 data segments for the bite force task and 1650 segments for the frequency task. Representative examples of the preprocessed signals are shown in Figure S16 (Supporting Information). For both classification tasks, a convolutional neural network (CNN) architecture was employed, consisting of two convolutional layers followed by two fully connected layers (Figure 4j). CNN was chosen for data processing due to its ability to automatically extract multi-scale spatiotemporal features from multi-channel STS triboelectric time-series signals, which often exhibit non-linear fluctuations and baseline drift. Its hierarchical feature extraction and localized receptive fields provide superior robustness to noise and signal variability compared with traditional machine learning models, making it well-suited for accurate and reliable bite force and frequency classification. The datasets were split into training, validation, and test sets, with five-fold cross-validation performed on the training/validation sets to comprehensively evaluate the model's generalization performance. The optimized CNN achieved an average classification accuracy of 98.67% for the bite force magnitude task and 98.82% for the frequency task across validation folds. The corresponding confusion matrices are presented in Figure 4k,l, confirming the model's robust predictive capability and generalizability across occlusal patterns.

To further evaluate the multi-channel STS's performance across different users, an extended in vivo study was conducted with six volunteers. As shown in Figure S17a (Supporting Information), the voltage heatmaps revealed consistent and distinguishable multi-channel responses across individuals, reflecting subject-specific occlusal force distributions. The averaged output performance across all participants (Figure S17b, Supporting Information) further confirmed the multi-channel STS's stability and reproducibility, with inter-individual variations remaining within a narrow range. These results collectively demonstrated the robustness of the multi-channel STS under diverse oral conditions. In addition, the subjective comfort evaluation from six volunteers, as shown in Figure S18 (Supporting Information), demonstrated consistently high scores across four dimensions (fit, pressure, irritation, and speech/swallowing

interference), with average ratings ranging from 4.0 to 5.0 on a 5-point Likert scale. Most participants reported good fit and negligible irritation (scores ≥ 4), while only one volunteer experienced minor speech interference. Overall, the results confirmed that the multi-channel STS provided high comfort, minimal functional disturbance, and strong suitability for intraoral applications.

3. Conclusion

In summary, we present a self-powered triboelectric sensor capable of real-time, 3D monitoring of occlusal forces, addressing longstanding challenges in intraoral sensing. By combining triboelectric transduction with a conformal, multilayer architecture and functionalized materials, the STS addressed the major limitations of conventional sensors. Specifically, the STS eliminates the need for invasive procedures and external power supply, while enabling full-vector force detection, including both normal and lateral shear components. This design ensures sensitive and reliable electrical signal generation under multi-directional loading, allowing accurate real-time monitoring of occlusal forces. The multi-channel design affords high spatial and temporal resolution, while ensuring biocompatibility and long-term operational stability. Importantly, coupling the platform with machine learning algorithms enables intelligent interpretation of complex occlusal signals, achieving accurate real-time classification and supporting personalized diagnostics. This triboelectric sensing strategy establishes a scalable framework for next-generation smart occlusal systems, with inherent compatibility for integration into wearable and implantable devices. Looking ahead, further efforts will focus on enhancing in vivo performance, expanding clinical validation, particularly in applications such as monitoring occlusal forces in dentures, orthodontic treatment, and temporomandibular disorder management, and advancing data analytics for early detection of conditions such as bruxism, malocclusion, and temporomandibular disorders. These directions highlight the practical significance of the STS platform for improving dental diagnostics and personalized oral care. Together, this work lays the foundation for intelligent, data-driven occlusal healthcare, advancing beyond the functional scope of existing sensing technologies.

4. Experimental Section

Synthesis of the PVDF-HFP/$BaTiO_3$ Composite Dielectric Layer: Poly(vinylidene fluoride-co-hexafluoropropylene) (PVDF-HFP, Sigma–Aldrich) was first dissolved in acetone at a concentration of 100 mg mL^{-1} under constant magnetic stirring at 50 °C for 2 h to ensure complete solubilization. Subsequently, $BaTiO_3$ nanoparticles (Sigma–Aldrich, <100 nm particle size) were added to the PVDF-HFP solution at designated weight ratios (3, 6, 9, 12, and 15 wt.%) to form the composite dielectric. The mixture was further ultrasonicated for 30 min and stirred for 2 h to achieve uniform dispersion. The resulting composite solution was then spin-coated onto a clean acrylic substrate at 2000 rpm for 60 s to obtain a uniform film. The coated substrate was placed in a vacuum oven and dried at 60 °C for 12 h to remove residual solvent and promote film crystallization.

Preparation of the Carbon–Silicone Composite Electrodes: Flexible conductive electrodes were prepared using a carbon–Ecoflex composite. Ecoflex 0030 (Smooth-On, Inc., USA) was prepared by mixing Part A and Part B in a 1:1 volume ratio and stirring thoroughly for 3 min. Carbon black powder (Cabot Vulcan XC72R) was then added to the prepolymer mixture at a volume ratio of 1:15 (carbon black:Ecoflex). The resulting mixture was stirred vigorously to ensure uniform dispersion of conductive particles within the elastomer matrix. The conductive mixture was then poured into a flat mold and cured at room temperature for 4 h, followed by post-curing at 60 °C for 2 h to enhance mechanical integrity. The cured carbon–silicone films were cut to the desired electrode dimensions for assembly.

Assembly of the STS Device: The fully cured carbon–silicone electrodes were aligned and laminated on both sides of the PVDF-HFP/$BaTiO_3$ composite dielectric layer using a thin layer of Ecoflex as adhesive to ensure mechanical compliance and minimize interfacial delamination. A layer of PU foam (5 mm thickness) was placed between the electrodes to act as a compressible spacer and mechanical buffer. The assembled multilayer structure was gently compressed to ensure conformal contact between layers, and then thermally bonded at 50 °C for 1 h under mild pressure to enhance structural stability. Electrical connections were made using copper wires adhered to the carbon–silicone electrode surfaces with conductive silver paste.

Oral Cavity Implementation of Multi-Channel STS: The multi-channel STS was tested in situ within the oral cavity. To ensure biocompatibility and hygiene, the PVDF-HFP/$BaTiO_3$ dielectric layer and the carbon-silicone electrode were fully encapsulated with a 0.5 mm thick disposable food-grade silicone film, preventing direct contact with the oral environment and bite forces. A new encapsulation film was applied before each test to maintain safety and cleanliness throughout the experiments. During testing, the sensor was positioned at the corresponding oral sites, and bite actions were recorded to obtain real-time multi-channel force measurements.

Participants of Experiments: A total of six volunteers were recruited for this study. All participants provided written informed consent prior to participation, and their involvement was entirely voluntary. Upon completion of the experiments, participants were offered small snacks as compensation.

Electric Measurement and Characterization: A linear motor was used to create alternative motions, and a programmable electrometer (Keithley 6514) and a data acquisition card (NI-6259) were used to measure the output voltage.

Supporting Information

Supporting Information is available from the Wiley Online Library or from the author.

Acknowledgements

This work was supported by the National Natural Science Foundation (Grant No. 22479016).

Conflict of Interest

The authors declare no conflict of interest.

Author Contributions

Y.D. and J.S. contributed equally to this work. D.W. and Z.L.W. proposed the idea and the project. D.W., X.L.D., and T.L.R. designed all the experiments and supervised the whole project. Y.D. carried out the experiments in this paper. Y.D. and J.K.S. analyzed the corresponding data. All the authors discussed the results and commented on the manuscript. D.W. and Y.D. wrote this paper.

Data Availability Statement

The data that support the findings of this study are available from the corresponding author upon reasonable request.

Keywords

machine learning algorithm, occlusal force, occlusal frequency, self-powered, triboelectric sensor

Received: July 29, 2025
Revised: August 30, 2025
Published online: November 20, 2025

[1] a) D. Ciavarella, M. Lorusso, C. Fanelli, D. Ferrara, M. Laurenziello, G. Montaruli, R. Esposito, M. Tepedino, *J. Oral Rehabil.* **2024**, *51*, 1813; b) M. Morokuma, Y. Yoneyama, R. Matsuda, T. Hosoi, C. Ohkubo, *J. Prosthodont.* **2015**, *24*, 532; c) H. Karibe, K. Ogata, Y. Hasegawa, K. Ogihara, *J. Oral Rehabil.* **2003**, *30*, 307.

[2] a) Z. Li, L. Wang, *Sci. Rep.* **2025**, *15*, 24502; b) T. H. Farook, T. M. Haq, L. Ramees, J. Dudley, *Sci. Rep.* **2024**, *14*, 16423; c) R. K. Al-Rokhami, K. A. Sakran, N. A. Al-Worafi, M. Al-balaa, A. Algahefi, Z. Li, *Sci. Rep.* **2025**, *15*, 24896.

[3] a) J. O. Agbaje, E. V. d. Casteele, A. S. Salem, D. Anumendem, E. Shaheen, Y. Sun, C. Politis, *Sci. Rep.* **2017**, *7*, 5356; b) Q. Wang, Z. Zhao, J. Li, R. Zhao, M. Zhou, K. Tang, S. Bai, C. Ma, F. Wang, *J. Oral Rehabil.* **2024**, *51*, 1675; c) *Br. Dent. J.* **2019**, *226*, 467.

[4] a) H. Wang, H. Chen, S. Tian, Y. Sun, F. Wu, *J. Esthet. Restor. Dent.* **2024**, *36*, 1258; b) R. S. Saini, S. A. Quadri, M. A. Kanji, R. I. H. Binduhayyim, A. Avetisyan, S. A. Mosaddad, A. Heboyan, *Evid. Based Dent.* **2025**, *26*, 148, https://doi.org/10.1038/s41432-025-01135-6; c) S.-B. Kim, K.-W. Lee, H. Bae, K.-H. Yi, K.-S. Hu, H.-J. Kim, *Sci. Rep.* **2025**, *15*, 22813.

[5] a) S. Cheng, B. Chen, Y. Zhou, M. Xu, Z. Suo, *Extrem. Mech. Lett.* **2020**, *34*, 100592; b) X. Sun, Z. Dai, Z. Zhang, X. Fan, Z. Fu, H. Zhu, R. Cai, K. Qian, *J. Mater. Chem. A* **2024**, *12*, 18423; c) J.-H. Liu, W.-D. Li, J. Jia, C.-Y. Tang, S. Wang, P. Yu, Z.-M. Zhang, K. Ke, R.-Y. Bao, Z.-Y. Liu, Y. Wang, K. Zhang, M.-B. Yang, W. Yang, *Nano Energy* **2022**, *103*, 107787; d) X. Jin, L. Li, S. Zhao, X. Li, K. Jiang, L. Wang, G. Shen, *ACS Nano* **2021**, *15*, 18385.

[6] W. Wang, J. Liu, N. Zhao, B. Yang, *Langmuir* **2023**, *39*, 13571.

[7] M. Zhu, Q. Shi, T. He, Z. Yi, Y. Ma, B. Yang, T. Chen, C. Lee, *ACS Nano* **2019**, *13*, 1940.

[8] Y.-W. Jang, J. Kim, J. Shin, J.-W. Jo, J. W. Shin, Y.-H. Kim, S. W. Cho, S. K. Park, *Adv. Mater.* **2024**, *36*, 2400614.

[9] a) H. G. Shin, W. K. Chung, K. Kim, *Nat. Commun.* **2025**, *16*, 5575; b) L. Qiao, X. Gao, K. Ren, C. Qiu, J. Liu, H. Jin, S. Dong, Z. Xu, F. Li, *Nat. Commun.* **2024**, *15*, 805.

[10] a) Y. Wang, C. Sun, D. Ahmed, *Nat. Electron.* **2025**, *8*, 485, https://doi.org/10.1038/s41928-025-01386-2; b) F. Yi, X. Wang, S. Niu, S. Li, Y. Yin, K. Dai, G. Zhang, L. Lin, Z. Wen, H. Guo, J. Wang, M.-H. Yeh, Y. Zi, Q. Liao, Z. You, Y. Zhang, Z. L. Wang, *Sci. Adv.* **2016**, *2*, 1501624.

[11] a) F.-R. Fan, Z.-Q. Tian, Z. L. Wang, *Nano Energy* **2012**, *1*, 328; b) J. Chen, Z. L. Wang, *Joule* **2017**, *1*, 480; c) Y. Wu, Y. Luo, J. Qu, W. A. Daoud, T. Qi, *Nano Energy* **2019**, *64*, 103948.

[12] a) L. Su, S. Kuang, Y. Zhao, J. Li, G. Zhao, Z. L. Wang, Y. Zi, *Sci. Adv.* **2024**, *10*, adq8989; b) F. Wang, Z. Ren, J. Nie, J. Tian, Y. Ding, X. Chen, *Adv. Mater. Technol.* **2020**, *5*, 1900789; c) X. Wei, B. Wang, X. Cao, H. Zhou, Z. Wu, Z. L. Wang, *Nat. Food* **2023**, *4*, 721; d) Y. Du, S. Fu, C. Shan, H. Wu, W. He, J. Wang, H. Guo, G. Li, Z. Wang, C. Hu, *Adv. Funct. Mater.* **2022**, *32*, 2208783; e) G. Xu, H. Wang, G. Zhao, J. Fu, K. Yao, S. Jia, R. Shi, X. Huang, P. Wu, J. Li, B. Zhang, C. K. Yiu, Z. Zhou, C. Chen, X. Li, Z. Peng, Y. Zi, Z. Zheng, X. Yu, *Sci. Adv.* **2025**, *11*, adt0318.

[13] a) X. Pu, H. Guo, J. Chen, X. Wang, Y. Xi, C. Hu, Z. L. Wang, *Sci. Adv.* **2017**, *3*, 1700694; b) Y. Du, P. Shen, H. Liu, Z. Zhang, T. Ren, R. Shi, Z. Wang, D. Wei, *Adv. Funct. Mater.* **2024**, *34*, 2409602; c) S. Wang, G. Xie, H. Tai, Y. Su, B. Yang, Q. Zhang, X. Du, Y. Jiang, *Nano Energy* **2018**, *51*, 231.

[14] Y. Du, Z. L. Wang, D. Wei, *Nano Energy* **2025**, *143*, 111292.

[15] a) F. Yin, Y. Guo, Z. Qiu, H. Niu, W. Wang, Y. Li, E. S. Kim, N. Y. Kim, *Nano Energy* **2022**, *101*, 107541; b) X. Zhang, Y. Yu, X. Xia, W. Zhang, X. Cheng, H. Li, Z. L. Wang, T. Cheng, *Adv. Energy Mater.* **2023**, *13*, 2302353.

[16] a) H. Yu, W. Cao, W. Han, W. Li, Y. Gao, Y. Zhang, F. Chen, S. Qi, *Nano Energy* **2025**, *133*, 110466; b) S. Panda, S. Hajra, H.-G. Kim, P. G. R. Achary, P. Pakawanit, Y. Yang, Y. K. Mishra, H. J. Kim, *ACS Appl. Mater. Interfaces* **2023**, *15*, 36096.

[17] H. Chen, Z. Su, Y. Song, X. Cheng, X. Chen, B. Meng, Z. Song, D. Chen, H. Zhang, *Adv. Funct. Mater.* **2017**, *27*, 1604434.

[18] W. Fan, R. Lei, H. Dou, Z. Wu, L. Lu, S. Wang, X. Liu, W. Chen, M. Rezakazemi, T. M. Aminabhavi, Y. Li, S. Ge, *Nat. Commun.* **2024**, *15*, 3509.

[19] a) S. Panda, S. Hajra, H. Jeong, B. K. Panigrahi, P. Pakawanit, D. Dubal, S. Hong, H. J. Kim, *Nano Energy* **2022**, *102*, 107682; b) J. Swain, A. Priyadarshini, S. Hajra, S. Panda, J. Panda, R. Samantaray, Y. Yamauchi, M. Han, H. J. Kim, R. Sahu, *J. Alloys Compd.* **2023**, *965*, 171438; c) J. Lee, S. Hajra, S. Panda, W. Oh, Y. Oh, H. Shin, Y. K. Mishra, H. J. Kim, *Int. J. Precis. Eng. Manuf.-Green Technol.* **2023**, *11*, 233.

[20] a) S. D. Almeida, J. C. Silva, J. P. M. R. Borges, M. C. Lança, *Macromol.* **2022**, *2*, 531; b) N. Bag, J. Roy, A. Chatterjee, D. Mondal, S. Ghosh, S. Aktar, S. Bhandary, S. Roy, S. Das, *Mater. Today Sustain.* **2025**, *30*, 100; c) V. Fathollahzadeh, M. Khodaei, S. Emadi, K. Hajisharifi, *Sci. Rep.* **2025**, *15*, 28515.

[21] a) Y. Du, P. Shen, H. Liu, Y. Zhang, L. Jia, X. Pu, F. Yang, T. Ren, D. Chu, Z. Wang, D. Wei, *Sci. Adv.* **2024**, *10*, adp8681; b) Y. Du, Z. Wang, D. Wei, *Sci. Bull.* **2025**, *70*, 1375.

[22] T. Deng, X. Zhang, Z. Yang, G. Xiang, *Sci. China Technol. Sci.* **2024**, *68*, 2001.